



# Mesoporous $\text{ZnFe}_2\text{O}_4@\text{TiO}_2$ Nanofibers Prepared by Electrospinning Coupled to PECVD as Highly Performing Photocatalytic Materials

Amr A. Nada, Maryline Nasr, Roman Viter, Philippe Miele, Stephanie Roualdes, Mikhael Bechelany

## ► To cite this version:

Amr A. Nada, Maryline Nasr, Roman Viter, Philippe Miele, Stephanie Roualdes, et al.. Mesoporous  $\text{ZnFe}_2\text{O}_4@\text{TiO}_2$  Nanofibers Prepared by Electrospinning Coupled to PECVD as Highly Performing Photocatalytic Materials. *Journal of Physical Chemistry C*, 2017, 121 (44), pp.24669 - 24677. 10.1021/acs.jpcc.7b08567 . hal-01674793

**HAL Id: hal-01674793**

**<https://hal.umontpellier.fr/hal-01674793>**

Submitted on 10 Jun 2021

**HAL** is a multi-disciplinary open access archive for the deposit and dissemination of scientific research documents, whether they are published or not. The documents may come from teaching and research institutions in France or abroad, or from public or private research centers.

L'archive ouverte pluridisciplinaire **HAL**, est destinée au dépôt et à la diffusion de documents scientifiques de niveau recherche, publiés ou non, émanant des établissements d'enseignement et de recherche français ou étrangers, des laboratoires publics ou privés.

# Mesoporous ZnFe<sub>2</sub>O<sub>4</sub>@TiO<sub>2</sub> Nanofibers Prepared by Electrospinning Coupled with PECVD as Highly Performing Photocatalytic Materials

Amr A. Nada<sup>1,2</sup>, Maryline Nasr<sup>2,3</sup>, Roman Viter<sup>4</sup>, Philippe Miele<sup>2,5</sup>, Stéphanie Roualdes<sup>2</sup>, Mikhael Bechelany<sup>2\*</sup>

<sup>1</sup>Dept. of Analysis and Evaluation, Egyptian Petroleum Research Institute, Cairo, Nasr city P.B. 11727, Egypt.

<sup>2</sup>Institut Européen des Membranes IEM, UMR 5635, ENSCM, Université de Montpellier, CNRS, Place Eugène Bataillon, CC047, F-34095 Montpellier Cedex 5, France

<sup>3</sup>EC2M, Faculty of Sciences 2, and Research Platform for Nanosciences and Nanotechnologies, Lebanese University, Campus Pierre Gemayel, Fanar, 90656 Lebanon.

<sup>4</sup>Institute of Atomic Physics and Spectroscopy, University of Latvia, 19 Raina Blvd., LV 1586 Riga, Latvia

<sup>5</sup>Institut Universitaire de France (IUF)

Corresponding author: [mikhael.bechelany@umontpellier.fr](mailto:mikhael.bechelany@umontpellier.fr)

## ABSTRACT

Zinc ferrite @ titanium dioxide (ZnFe<sub>2</sub>O<sub>4</sub>@TiO<sub>2</sub>) composite nanofibers were elaborated by combining the two different techniques: electrospinning and plasma enhanced chemical vapour deposition (PECVD). The nanofibers compositions were controlled using different ratio of zinc to iron. Their structural, morphological, and optical properties were analysed by scanning electron microscopy (SEM), X-ray diffraction (XRD), energy-dispersive X-ray spectroscopy (EDX), BET surface area, Raman spectroscopy and UV-Visible

spectrophotometry. The photocatalytic activity has been investigated by the degradation of methylene blue (MB) under visible light. The results indicate that the combination of spinel structure with titanium dioxide improves the photodegradation up to 98%. The deposition of  $\text{TiO}_2$  via PECVD on zinc ferrite enhances the absorption of  $\text{TiO}_2$  into the visible region and increases the electron-hole separation. In addition, the improved surface area can promote adsorption, desorption and diffusion of reactants and products, which is favourable to obtain a high photocatalytic activity.

## INTRODUCTION

The development of the dye industries throughout the planet has led to increase water contamination <sup>1-2</sup>, which implies a serious threat to humans and environment. Therefore, many strategies have been developed in order to remove the organic dyes from wastewater such as chemical flocculation <sup>3</sup>, adsorption and ion exchange <sup>4-6</sup>. However, the traditional remediation of dye wastewater has many side effects including the secondary pollution, the low degradation rate and the long processing cycle <sup>7-8</sup>.

As an alternative approach, photocatalysis has attracted much attention due to its ability to degrade the organic dye in wastewater into environmental friendly compounds such as  $\text{CO}_2$  and water <sup>9-10</sup>. Many researchers have focused on semiconductors materials such as  $\text{TiO}_2$  and  $\text{ZnO}$ , due to their high photocatalytic activity <sup>11-12</sup>. Among these materials, the spinel structure Zinc ferrite ( $\text{ZnFe}_2\text{O}_4$ ) has been widely investigated due to its several potential applications, such as gas sensor, electrocatalyst as well as its photocatalytic properties <sup>13-16</sup>. All applications of zinc ferrite are mainly dependent on its surface area and morphology. Thus, many methods have been employed to elaborate different morphologies of zinc ferrite such as core-shell, nanoparticles and nanofibers by hydrothermal, co-precipitation and electrospinning technique, respectively<sup>17-19</sup>. In particular, zinc ferrite nanofibers were

synthesised by electrospinning for different applications such as: (i) Preparation of NiZn-ferrite nanofibers by electrospinning for DNA separation <sup>20</sup>, (ii) Electrospinning synthesis of ZnFe<sub>2</sub>O<sub>4</sub>/Fe<sub>3</sub>O<sub>4</sub>/Ag nanoparticle-loaded mesoporous carbon fibers with magnetic and photocatalytic properties <sup>21</sup>, (iii) Electrospun ZnFe<sub>2</sub>O<sub>4</sub>-based nanofiber composites with enhanced super capacitive properties <sup>22</sup> and (iv) Electrospinning synthesis of Ni, Fe co-doped ultrafine-ZnFe<sub>2</sub>O<sub>4</sub>/C nanofibers for lithium ion storage <sup>23</sup>.

Spinel ZnFe<sub>2</sub>O<sub>4</sub> is a low band gap, thus it can be excited by visible light for the degradation of organic pollutants <sup>24-25</sup>. However, the poor separation efficiency of photo-generated electrons and holes in the ZnFe<sub>2</sub>O<sub>4</sub> leads to a low photocatalytic activity <sup>26</sup>. The efficiency can be improved by loading different metals such as Ag or Al on the surface of ZnFe<sub>2</sub>O<sub>4</sub> <sup>27-28</sup>. On another hand, titanium dioxide has attracted attention as a photocatalyst (in dye sensitized solar cells, water splitting, self-cleaning and degradation of organic pollutant) due to its relatively low cost, high stability and low toxicity.<sup>29-30</sup> However, the high recombination rate between the electron-hole of TiO<sub>2</sub> limits the efficiency of the photocatalytic reaction. In addition, TiO<sub>2</sub> has a wide band gap (3.2 eV) and it can only be excited by UV light. Therefore, the use of solar light which contain 44% of visible light and 7% of UV light appears to be quite difficult <sup>9, 31</sup>. In order to shift the absorption edge of TiO<sub>2</sub> to the visible range, several processes have been carried out, such as (i) Conjugation with semiconductor that has small band gap <sup>32-34</sup>, (ii) Addition of transition metals <sup>35-36</sup>, (iii) Doping with non-metal elements <sup>37-38</sup>, (iv) Co-catalyst loading <sup>39-43</sup> and (v) Mesoporous silicon nanopillars (NPL) <sup>44</sup>.

In this paper, electrospinning and Plasma-Enhanced Chemical Vapour Deposition (PECVD) techniques have been combined to produce special forms of ZnFe<sub>2</sub>O<sub>4</sub>@TiO<sub>2</sub> nanofibers. Among all techniques used to prepare zinc ferrite, electrospinning is a simple and cost-effective technique. It permits the synthesis of nanofibers with controllable diameters ranging

from a few to several hundred nanometers.<sup>45-46</sup> Mesoporous structure could be also obtained depending on processing conditions. In addition, plasma processes are very competitive to insure stability, integrity and compactness of the material. Among plasma processes, Plasma-Enhanced Chemical Vapour Deposition (PECVD) is a very promising low-temperature one-step method for deposition and stacking of TiO<sub>2</sub> onto nanofibers substrates. This versatile method enables optimization of structural and functional properties of composite to get promising materials. In the present work, the plasma enhanced chemical vapour deposition (PECVD) method has been applied for the first time to elaborate ZnFe<sub>2</sub>O<sub>4</sub>@TiO<sub>2</sub> mesoporous nanofibers with high surface area. The structural, morphological and optical properties of the prepared samples have been analyzed. The performance of these materials for photocatalytic degradation of methylene blue under visible light has also been evaluated.

## EXPERIMENTAL SECTION

### 1. Chemicals and materials

Zinc nitrate hexahydrate (99.99%, 228737), Iron(III) nitrate nonahydrate (99.99%, 216828), titanium tetra-isopropoxide (TTIP) Ti(OCH(CH<sub>3</sub>)<sub>2</sub>)<sub>4</sub> (97%, 205273), polyvinylpyrrolidone (PVP) (Mw = 1 300 000 g/mol) (437190), acetic acid (98%, 33209), (DMF) N,N-dimethylformamide (99.8%, 33120) and methylene blue (MB) (M9140) were purchased from Sigma Aldrich, and used without any further purification. Absolute ethanol (99%, 20821.310) was purchased from VWR PROLABO Chemicals.

### 2. Preparation of zinc ferrite nanofibers

The zinc combined with iron nanofibers was prepared by the electrospinning technique.<sup>47-48</sup> The polymer solution was prepared as follows: 1 g of PVP was dissolved in 9 mL of absolute ethanol. Then, different molar ratios of Zn:Fe (1:0, 1:1, 1:2 and 1:3) were used to fabricate

nanofibers with different amounts of Zn and Fe. The naming of the samples ZF0, ZF1, ZF2 and ZF3 refers to [Z – zinc and F – iron] . Numbers 0, 1, 2 and 3 were referred to different molar ratios of Zn:Fe (1:0, 1:1, 1:2 and 1:3) respectively. Zinc nitrate and iron nitrate were completely dissolved in 5 mL of N,N-dimethylformamide (DMF) with vigorous stirring to form a homogeneous solution. 0.8 mL of metal-DMF was added dropwise to the PVP solution with low stirring for 2 hours. Finally, 1 mL of acetic acid was added to the mixture with low stirring for 1 hour. The homogeneous solution was typically extruded through a stainless steel nozzle with a diameter of 0.7 mm at a constant flow rate of 0.5 ml/h. The feeding flow rate was controlled by a syringe pump. The temperature inside the electrospinning chamber was fixed around  $38 \pm 5^{\circ}\text{C}$ . The nanofibers were collected on a rotating coil covered with an aluminium foil with a rotation speed of 400 rpm. A high voltage of 1.8 KV/cm was applied. In the electrospinning process, a high applied voltage was achieved by connecting the positive and ground terminals to the nozzle and the metallic collector, respectively. During the electrospinning, the applied electric field overcomes the surface tension of the polymeric solution, that way ejecting a continuous jet which upon subsequent solvent evaporation and bending produces nanofibers on the collector surface.

### **3. Deposition of TiO<sub>2</sub> by PECVD (Plasma Enhanced Chemical Vapour Deposition)**

Before deposition, the base pressure in the chamber was maintained at 1 Pa by pumping. The liquid precursor titanium tetra-isopropoxide (TTIP) was maintained in an oil bath at 80 °C. The inert argon was bubbling in the TTIP liquid as a carrier gas; the carrying line was heated at 100 °C in order to avoid any condensation of the precursor. Oxygen was introduced as an oxidant gas. R.F. power generator (CESARTM 136) coupled with a matching box (RF Navio, Advanced Energy) was connected to an inner electrode (diameter 10 cm) on top of the chamber. The bottom electrode (diameter 10 cm) and the chamber body were grounded. The

substrate (i.e. bottom electrode) was heated with a heating device (Eurotherm) up to 150° C. The optimum sample ZF2 was used as substrate in a 7 cm a hollow stainless steel dish. The oxygen partial pressure controlling the oxygen flux was set to 0.17 mbar. The partial pressure of TTIP mixed with Ar was 0.225 bars. The distance between the two electrodes ( $d_p$ ) was 3.0 cm and the discharge power equal to 50 W. The deposition time was 1 h to produce ZF2T. Schematic diagram of plasma reactor is presented in Figure S1. All prepared composite nanofibers were collected and then calcined in a furnace at 550° C with a heating rate of 1° C/min for 3 h in air.

#### **4. Characterisations of materials**

The crystalline phase of the materials was analysed by X-ray diffraction (XRD), using a PANalytical Xpert-PRO diffractometer equipped with an Xcelerator detector using Ni-filtered Cu-radiation ( $\lambda = 1.54 \text{ \AA}$ ). The scan step size was fixed to 0.0167 °/step and the time per step was 0.55 sec/step. Raman spectra were obtained from Horiba XploRA,  $\lambda = 659 \text{ nm}$  at a power of 20 W with the following acquisition conditions: continuous mode time of 10 seconds, snapshot time of 7 seconds, number of accumulations set to 30 time and a microscope objective lens of 100x. Scanning electron microscopy (SEM) images were taken with a Hitachi S4800, Japan. Energy-dispersive X-ray spectroscopy analysis (EDX) and elemental mapping were performed with a Zeiss EVO HD15 microscope coupled with an Oxford X-MaxN EDX detector. The UV-VIS absorbance spectra were recorded by a Jasco V-570 UV-VIS-NIR spectrophotometer. The surface area of the samples was determined from nitrogen adsorption–desorption isotherms at liquid nitrogen temperature using Micromeritics ASAP 2010 equipment (outgassing conditions: 200°C – 12 h).

#### **5. Photocatalytic reaction**

20 mg of each photocatalyst was added into 20 mL of MB aqueous solution ( $C = 20 \text{ mg/L}$ ). MB was used as a reference for organic pollutants. The mixture was magnetically stirred in the dark for 30 min before light irradiation in order to establish the adsorption–desorption equilibrium. Then, the mixture was irradiated by a 500 W linear halogen lamp (the wavelength distribution was in visible region) under continuous stirring. The emission spectrum of the halogen lamp is in the range 420 to 600 nm.<sup>49</sup> The reaction temperature was kept constant at 25° C by circulating water in a cylindrical tube surrounding the photo-reactor during the entire experiment. The distance between the lamp and the dye solution was maintained at 10 cm. Every 30 min, 2 mL of the sample solution was taken out and centrifuged to remove the catalyst. The centrifuged solutions were analysed by a UV-VIS spectrometer. The photocatalytic degradation efficiency was calculated as follows:

$$\text{Degradation efficiency (\%)} = (C_0 - C)/C_0 * 100 \quad \text{equation (1)}$$

Where  $C_0$ , is the initial concentration of the dye before degradation and  $C$ , is the final concentration of the dye after degradation<sup>50</sup>.

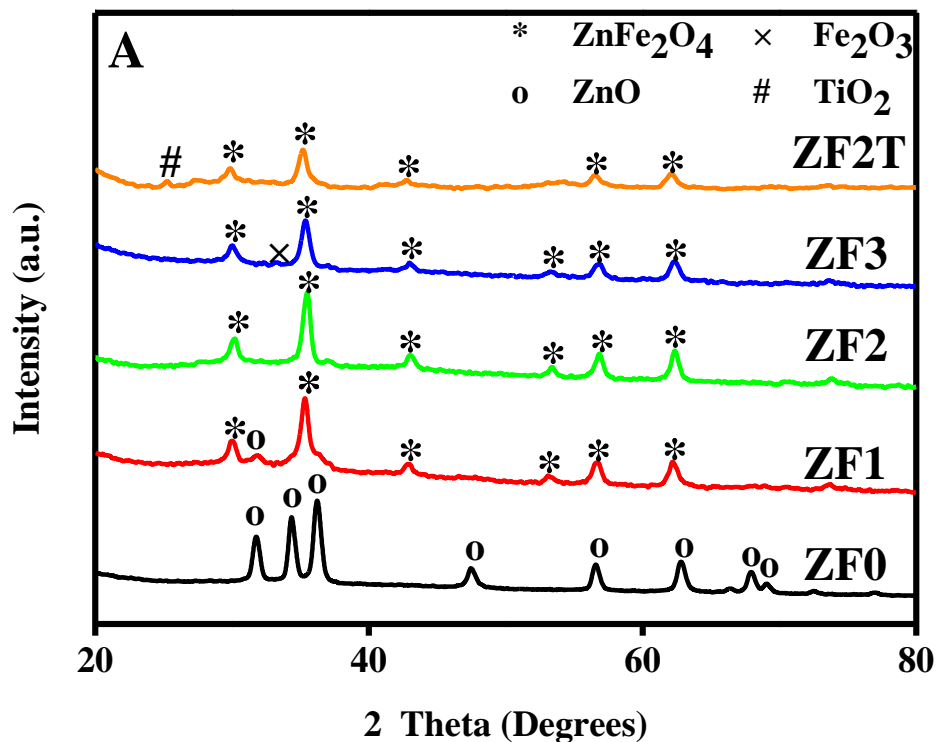
## RESULTS AND DISCUSSION

The XRD patterns of all prepared materials ZF0, ZF1, ZF2, ZF3 and ZF2T are presented in Figure 1. It can be seen that ZF0 has peaks characteristic of the ZnO phase (JCPDS No. 01-089-1397) with major lattice planes structure (100), (002) and (101) corresponding to  $2\theta = 31.77^\circ$ ,  $34.34^\circ$  and  $36.23^\circ$  respectively. The disappearing of (002) and (101) planes in ZF1 is due to the overlapping with the (311) plane at  $2\theta = 35.33^\circ$  of the franklinite  $\text{ZnFe}_2\text{O}_4$ . In ZF2, the pure phase of  $\text{ZnFe}_2\text{O}_4$  was detected (JCPDS No. 00-022-1012)<sup>51-53</sup>. For ZF3, the peak at  $2\theta = 33^\circ$  corresponds to  $\text{Fe}_2\text{O}_3$  and is related to the major plane (222) of iron oxide (JCPDS No. 00-039-0238). When  $\text{TiO}_2$  was deposited on ZF2 (ZF2T sample), the main peak of anatase was detected at  $2\theta = 25.2^\circ$  related to the (101) plane (JCPDS No. 00-021-1272). In



the case of ZF2T, the broad peak at  $53^\circ$  is obtained from the overlapping of franklinite peaks at  $53.1^\circ$  and  $56.6^\circ$  with anatase peaks at  $53.9^\circ$  and  $55.1^\circ$ . The franklinite peaks are shifted to low angle in ZF2T sample compared with tZF2 sample (Figure 1b). This shift is certainly due to the formation of  $\text{TiO}_2$  on the surface of  $\text{ZnFe}_2\text{O}_4$ . Moreover it can be supposed that the incorporation of  $\text{Ti}^{4+}$  ions in the  $\text{ZnFe}_2\text{O}_4$  lattice did not happen in this case because the incorporation of  $\text{Ti}^{4+}$  should induce a shift to higher angle since the radius of  $\text{Zn}^{2+}$  (0.074 nm) and  $\text{Fe}^{3+}$  (0.0645 nm) is larger than that of  $\text{Ti}^{4+}$  (0.0605 nm) <sup>51</sup>.

The crystallite average sizes of zinc ferrite with different amounts of iron were estimated using the Scherrer equation <sup>9</sup>. The calculated results (Table 1) show that the crystallite sizes are decreasing with the increasing of iron ratio. We can suggest that the iron is a grain-growth inhibitor for the franklinite  $\text{ZnFe}_2\text{O}_4$  from ZF1 to ZF3.



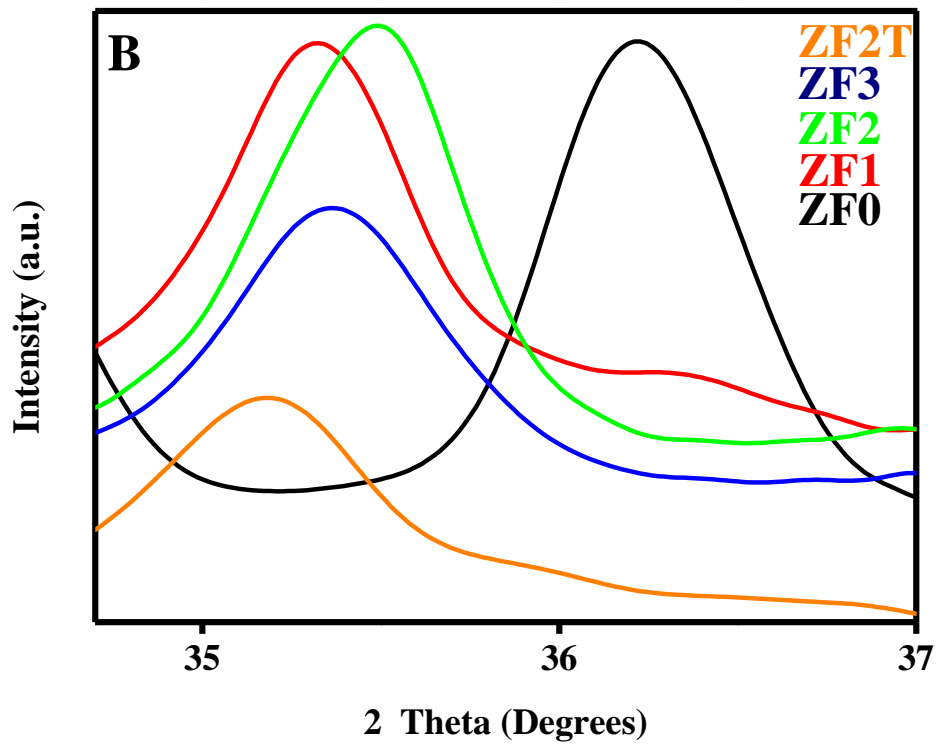


**Figure 1.** XRD patterns of all prepared nanofibers ZF0, ZF1, ZF2, ZF3 and ZF2T on the  $2\theta$  range  $20-80^\circ$  (A) and on the  $2\theta$  range  $34-37^\circ$  (B).

**Table 1.** Grain size of zinc ferrite with different iron ratios

	ZF1	ZF2	ZF3	ZF2T
Grain size (nm)	20.6	19.6	19.1	17.0

The obtained materials were characterized as well by Raman spectroscopy (Figure 2). In ZF0, the observed peak at  $437.32\text{ cm}^{-1}$  was attributed to the  $E_{2h}$  mode which is the strongest mode in the ZnO wurtzite crystal structure. The peak at  $586.7\text{ cm}^{-1}$  corresponds to  $E_{1L}$  mode of ZnO<sup>52</sup>. In addition to these first-order modes, the Raman spectra also show another peak at  $327.29\text{ cm}^{-1}$ , which is attributed to a combination of the first-order modes and an overtone, identified

as M point phonons  $2-E_2(M)$  of ZnO. From Figure 2, it is clear that the formation of  $ZnFe_2O_4$  leads to the decrease of the  $E_{2h}$  intensity. In addition, the broad peak at  $615.33\text{ cm}^{-1}$  in ZF1 sample can be attributed to the spinel structure of ferrite  $ZnFe_2O_4$ . This peak refers to the  $A_{1g}$  mode of the symmetric stretch of tetrahedral  $FeO_4$  <sup>51</sup>. In ZF2,  $E_{2h}$  mode disappears indicating the formation of pure phase of zinc ferrite. The  $E_g$  that appears at  $333.5\text{ cm}^{-1}$  is due to the symmetric bending of oxygen ions with respect to Fe <sup>53</sup>. After deposition of  $TiO_2$  on ZF2 (ZF2T sample), all the vibrations modes of anatase appear at  $144.8\text{ cm}^{-1}$  ( $E_g$ ),  $198\text{ cm}^{-1}$  ( $E_g$ ),  $395.2\text{ cm}^{-1}$  ( $B_{1g}$ ),  $514\text{ cm}^{-1}$  ( $A_{1g}$ ) and  $634\text{ cm}^{-1}$  ( $E_g$ ) <sup>54</sup>. Beside the  $E_g$  band of zinc ferrite at  $329.1\text{ cm}^{-1}$  is observed. The broad peak at  $634\text{ cm}^{-1}$  ( $E_g$ ) has been blue shifted in comparison with the previous studies of Vahtrus *et al.* (2015) <sup>54</sup>. This shifting is attributed to the overlapping with zinc ferrite peak at  $615.33\text{ cm}^{-1}$ .

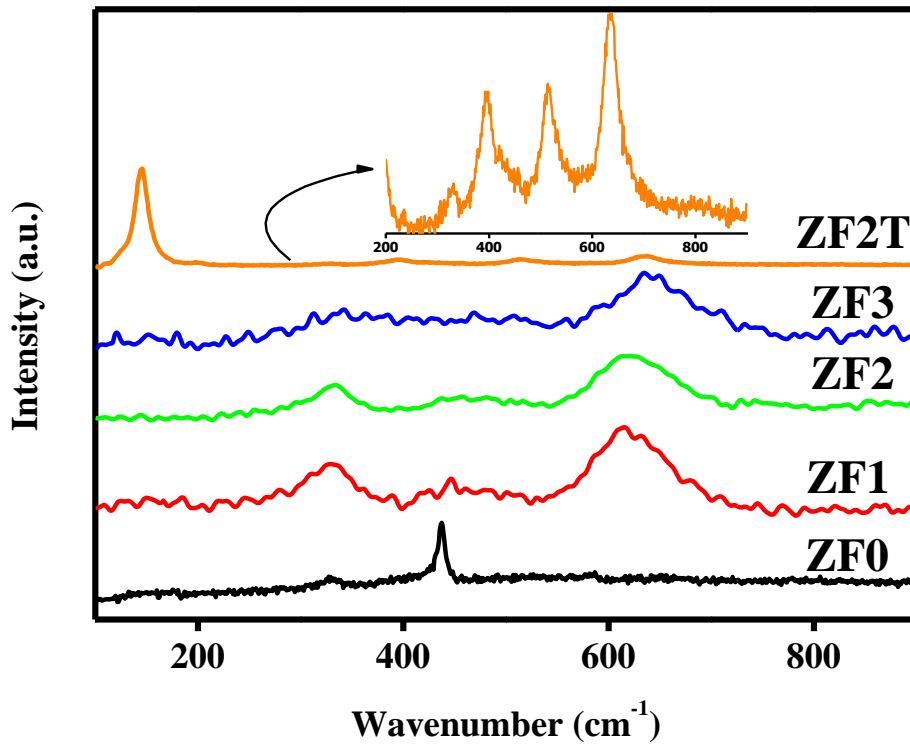


**Figure 2.** Raman shift of ZF0, ZF1, ZF2, ZF3 and ZF2T samples.

Scanning electron microscopy was used to investigate the morphological features of the prepared nanofibers. It was found that the morphology of the prepared nanofibers strongly depends on the Zn/Fe ratio, as presented in Figure 3. ZF0 sample presents a rod like morphology whereas ZF1 sample presents a nanofiber morphology. With a further increase of iron concentration (ZF2 and ZF3 samples), ZnFe<sub>2</sub>O<sub>4</sub> with an optimum nanofibers structure was obtained (Figure 3). The obtained nanofibers in ZF2T after TiO<sub>2</sub> deposition are shorter than ZF2 due to the plasma impact on the fibers. However, the fibers morphology is still preserves.

Furthermore, Ti, Fe, Zn and O elements were detected in EDX mappings for ZF2T, as presented in Figure S2. The distribution of TiO<sub>2</sub> is uniform on the surface of ferrite nanofibers. The composition presented in **Table 2** confirms the formation of ZnFe<sub>2</sub>O<sub>4</sub>@TiO<sub>2</sub> nanofibers.

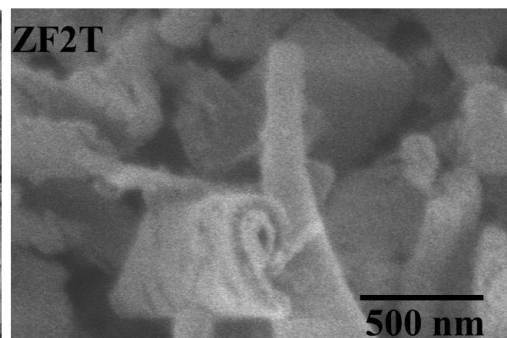
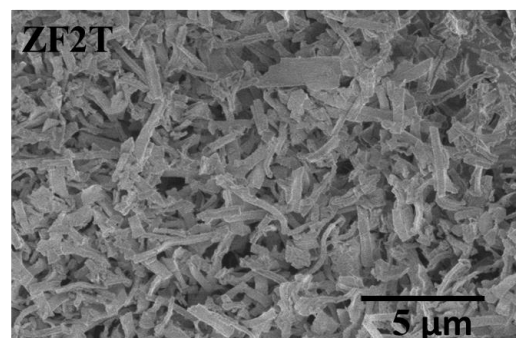
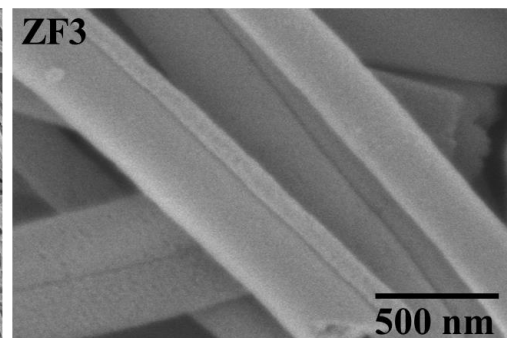
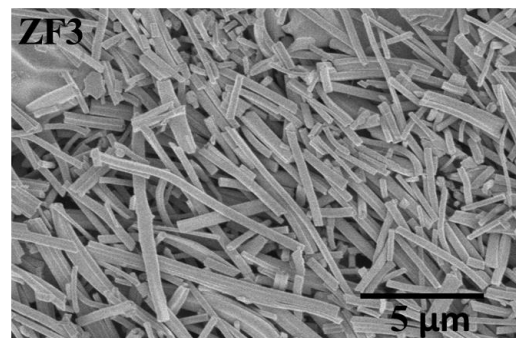
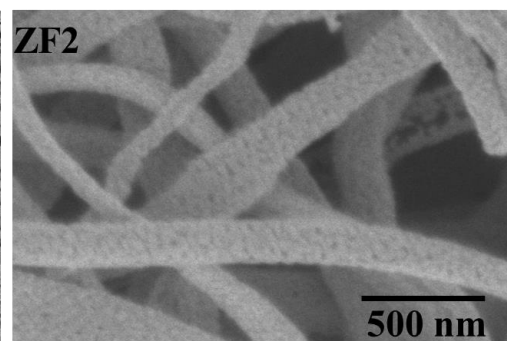
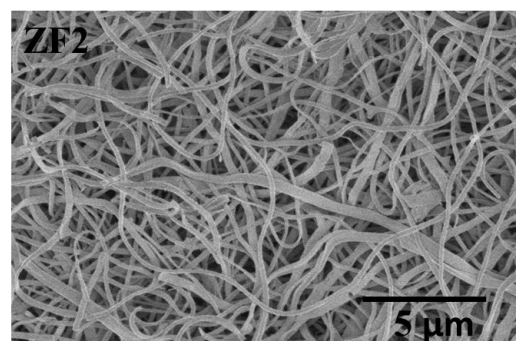
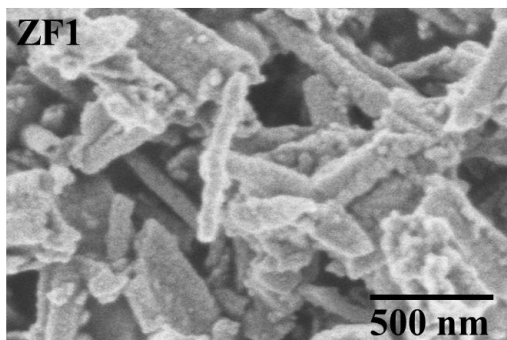
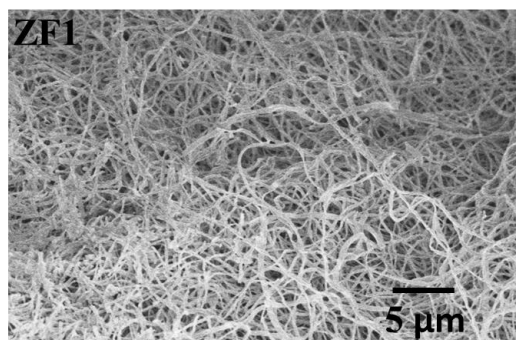
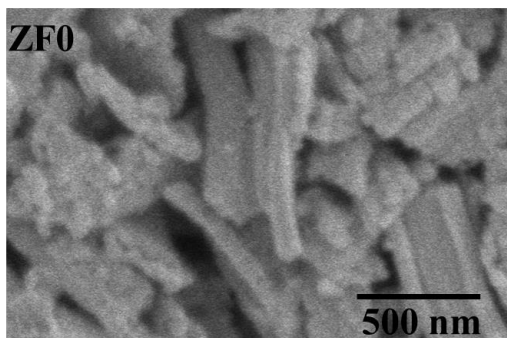
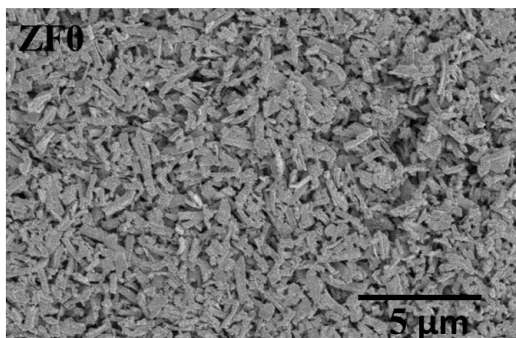


**Figure 3.** Scanning electron microscope images of ZF0, ZF1, ZF2, ZF3 and ZF2T samples.

**Table 2.** EDX data showing the composition of ZF2T.

Element	Atomic % (error: 1%)
O	67.5
Ti	8.5
Fe	16.3
Zn	7.7

The surface properties and pore structure parameters of the prepared samples were studied using nitrogen adsorption/desorption isotherm. The Barrett–Joyner–Halenda (BJH) pore size distribution is illustrated in Figure S2. From BET (Barrett–Emmett–Teller) method, we found a surface area of 31.18, 59.38, 77.86, 61.83 and 158.51 m<sup>2</sup>/g for ZF0, ZF1, ZF2, ZF3 and ZF2T, respectively. As shown in Figure S3, the isotherms of ZF2 and ZF2T are of type IV and display a distinct hysteresis loop, which indicates the mesoporous structure of the samples<sup>55</sup>. It is clear that the ZF2T has a high specific surface area (158.51 m<sup>2</sup>/g) and it maintains the multi-porosity of ZF2 nanofiber with enriched average pore volume (from 0.009 to 0.046 cm<sup>3</sup>/g). This could result from the elimination of PVP in ZF2 nanofibers during the TiO<sub>2</sub> plasma deposition. Such mesoporous structure with a very high surface area has not been recorded before for this material. This composite material can certainly promote adsorption, desorption and diffusion of reactants and products, which is favourable to obtain a high photocatalytic activity<sup>56</sup>. This composite ZF2T has a wide pore size distribution in the range of 2 to 11 nm, which might be beneficial for the adsorption of contaminant molecules in the liquid system. Moreover, the well-defined transport path of multi-porous ZF2T nanofibers is helpful for charge carrier.

The photocatalytic activity is controlled by the four mechanisms: the photoabsorption, the generation of electron-hole pairs, the charge carrier transfer and the charge carrier's utilization. ZF2T has the best absorption properties as confirmed in BET data. In another hand, the enhancement of the photocatalytic activity is mainly caused by the efficient generation and the transfer of the electron-hole pairs, which depend on the band gap structure of the photocatalyst.

The band gap of samples ( $E_g$ ) was determined by the following equation:

$$\alpha h\nu = A(h\nu - E_g)^{n/2} \quad \text{equation (2)}$$

where  $\alpha$  is the absorption coefficient,  $\nu$  is light frequency and  $n$  is a proportionality constant. The value of  $n$  is determined by the transition of semiconductor, i.e. direct transition as for zinc ferrite ( $n = 1$ ) or indirect transition as for  $\text{TiO}_2$  ( $n = 4$ ). The diffuse reflectance of all prepared samples is presented in Figure 4. In addition, the absorption edge of ZF2T had relatively steep edges, indicating that the absorption in the visible region was not due to the surface states but rather to an intrinsic band transition<sup>57</sup>. The  $E_g$  values of all samples are listed in Table 3. Where  $E_{g1}$  of ZF0 was presented for  $\text{ZnO}$ ,  $E_{g1}$  of ZF2T (IT) – indirect transitions for  $\text{TiO}_2$ ,  $E_{g2}$  values were displayed for  $\text{ZnFe}_2\text{O}_4$  and  $E_{g3-5}$  were referred to  $\text{Fe}_2\text{O}_3$ . These results indicate that ZF2T composites could absorb more photons which enhance the photocatalytic process.

Furthermore, the conduction band ( $\Delta E_C$ ), the valence band gap offsets ( $\Delta E_V$ ), the fermi level ( $E_F$ ) and the built in potential ( $V_{bi}$ ) are calculated in Table 4 by the following equations:<sup>58</sup>

$$\Delta E_C = \mathcal{K}_2 - \mathcal{K}_1 \quad \text{equation (3)}$$

$$\Delta E_V = E_{g1}(\text{IT}) - E_{g1}(\text{DT}) - \Delta E_C \quad \text{equation (4)}$$

$$E_F = \phi - \mathcal{K} \quad \text{equation (5)}$$

$$V_{bi} \cdot q = E_{F2} - E_{F1} \quad \text{equation (6)}$$

Where,  $\chi_{1,2} = 4.35$  and  $4.19$  eV are electron affinity values of zinc ferrite and  $\text{TiO}_2$ , respectively.<sup>59</sup>  $E_{g1}(\text{IT})$  and  $E_{g1}(\text{DT})$  are the band gap values from Table 3.  $\phi$  is the work function presented in Table 4.<sup>60</sup>  $q$  is electron charge and  $E_{F1,2}$  are Fermi level positions of  $\text{TiO}_2$  and zinc ferrite, respectively.

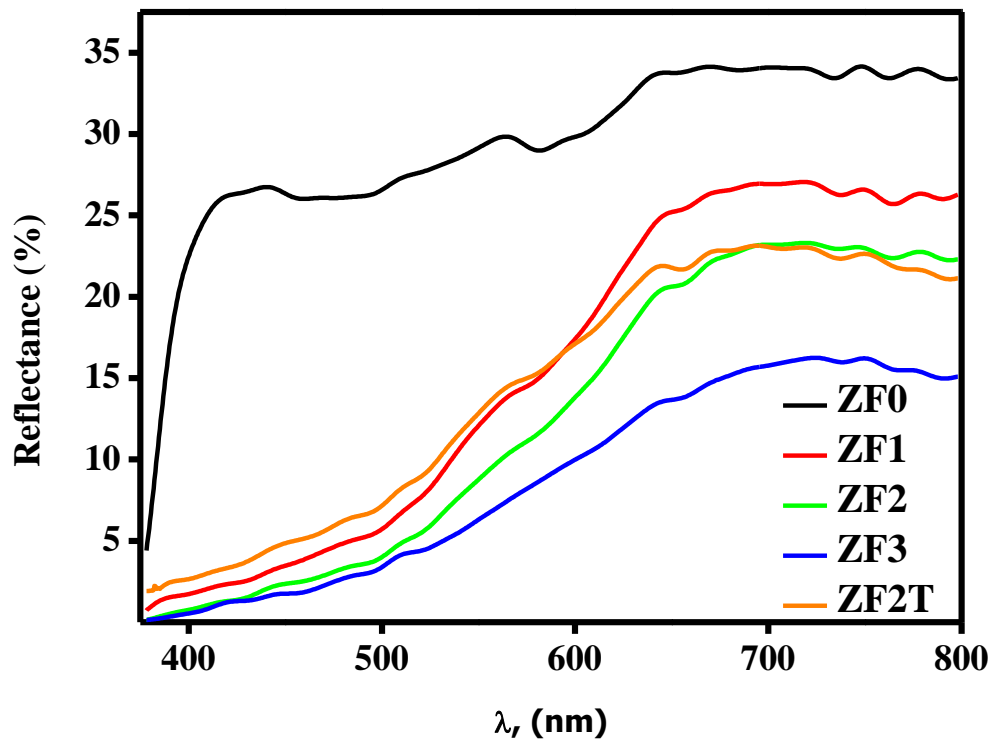


**Figure 4.** Diffuse reflectance of all prepared nanofibers.

**Table 3.** Band gap energy of ZF0, ZF1, ZF2, ZF3 and ZF2T nanofibers.

Sample Name	$E_{g1}$ (ev)	$E_{g2}$ (ev)	$E_{g3}$ (ev)	$E_{g4}$ (ev)	$E_{g5}$ (ev)
ZF0	3.22	--	--	--	--
ZF1	2.79	2.7	2.52	2.33	2.27
ZF2	2.85	2.7	2.53	2.33	2.27



ZF3	--	2.73	2.51	2.33	2.27
ZF2T (DT)*	2.78	2.73	2.48	--	2.26
ZF2T (IT)*	3.27 (TiO <sub>2</sub> )	--	--	--	--

\* ZF2T (DT) – direct transitions and ZF2T (IT) – indirect transitions

**Table 4.** Electronic parameters of ZF2T nanofibers.

	Electron affinity (eV)	Band gap (eV)	Work function (eV)	$\Delta E_C$ (eV)	$\Delta E_V$ (eV)	$V_{bi}$ (eV)
Zinc ferrite	4.35 <sup>59</sup>	2.78	4.56 <sup>59</sup>	0.16	0.33	0.02
TiO <sub>2</sub>	4.19 <sup>59</sup>	3.27	4.38 <sup>59</sup>			

The photoluminescence spectra of all prepared samples are shown in Figure 5. A drastic quenching of PL intensity of ZF2T was observed after the introduction of TiO<sub>2</sub> with zinc ferrite, indicating that the recombination of the photo-generated charge carriers was greatly reduced in the obtained materials.<sup>60</sup> This phenomenon could be attributed to the phase transitions. As it can be seen, the wavelength of the peak was shifted in ZF1 sample due to the disappearing of ZnO. This result matches well with the XRD data presented above.

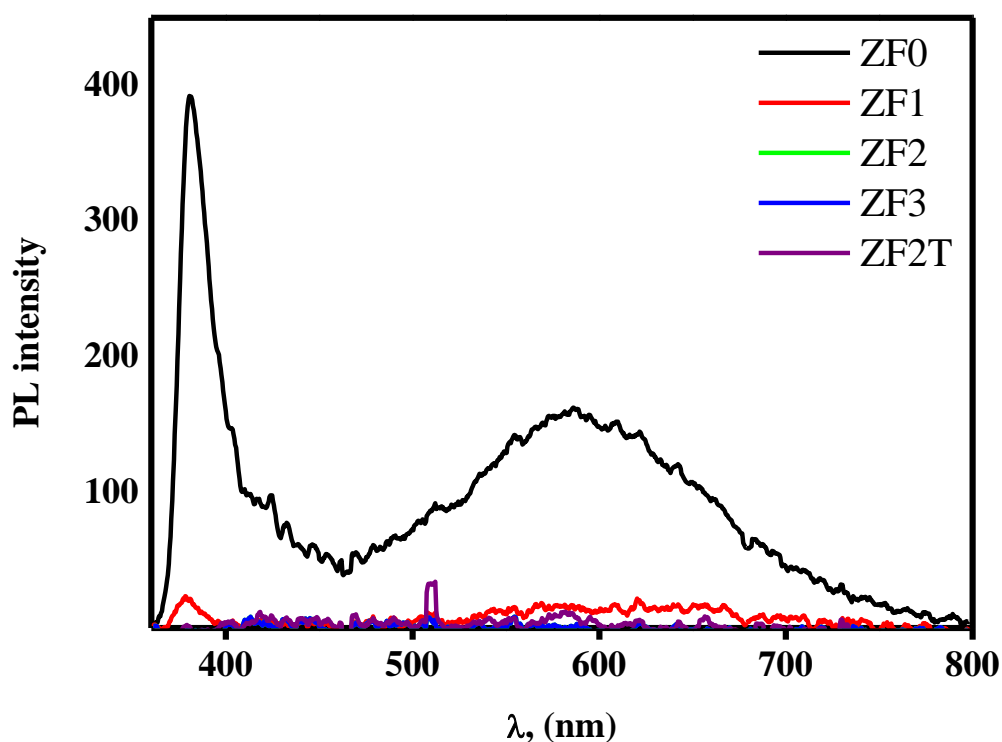


**Figure 5.** Photoluminescence of ZF0, ZF1, ZF2, ZF3 and ZF2T nanofibers.

The photocatalytic activities of zinc ferrite with different ratios of iron with or without deposition of titanium dioxide by PECVD were evaluated for the degradation of methylene blue under visible light. The MB is difficult to be photodegraded in the absence of a photocatalyst as shown in Figure 6. After 30 minutes in dark, the adsorption-desorption equilibrium was established as presented in Figure S4. The degradation of MB is up to 15%, 40%, 50%, 38% and 98% for ZF0, ZF1, ZF2, ZF3 and ZF2T respectively (Figure 6). It is well known that the enhancement of the photocatalytic activity depends on the specific surface area, crystallinity, light absorption capacity and separation efficiency of electron-hole pairs.<sup>61-62</sup> Therefore, the good photocatalytic activity of the ZF2T sample is directly related to its high surface area and quenching of photoluminescence due to the effect of spinel structure with TiO<sub>2</sub>. Moreover, a very high surface area has previously been recorded for this material

(ZnFe<sub>2</sub>O<sub>4</sub>@TiO<sub>2</sub> nanofibers) in comparison with the previously studied ZnFe<sub>2</sub>O<sub>4</sub>/TiO<sub>2</sub> nanoparticles (surface area : 36 m<sup>2</sup>/g).<sup>63</sup> The enhancement of surface area is another reason for the improvement of the photocatalytic activity.

The photodegradation rate was clarified by the degradation kinetic linear curves which are presented in Figure 7. The photodegradation reactions follow a Langmuir Hinshelwood first order kinetics model. The equation is described as follow:

$$r = dC/dT = kKC/(1+KC) \quad \text{equation (7)}$$

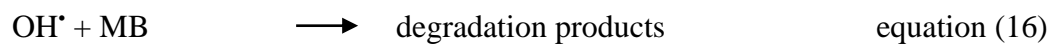
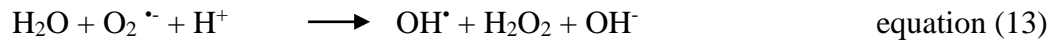
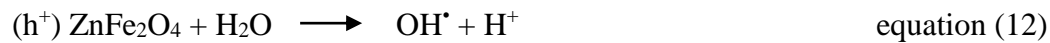
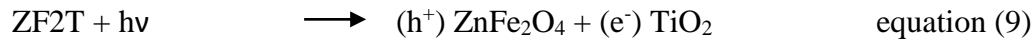
Where  $r$  is the rate of MB degradation (mg L<sup>-1</sup> min<sup>-1</sup>),  $C$  is the concentration of the MB solution (mg L<sup>-1</sup>),  $t$  is the degradation time,  $k$  is the reaction rate constant (mg L<sup>-1</sup> min<sup>-1</sup>), and  $K$  is the adsorption coefficient of MB (mg L<sup>-1</sup>). The relationship between  $\ln(C_0/C)$  and the reaction time ( $t$ ) shows that the decomposition of MB with different photocatalysts follows a pseudo first order kinetic:

$$\ln(C_0/C) = kKT = k_a t \quad \text{equation (8)}$$

where  $k_a$  is the apparent first-order rate constant (min<sup>-1</sup>) and  $C$  is the concentration at time  $t$ .  $k_a$  reported in Table 5 is obtained from the linear dependence between  $\ln(C_0/C)$  and time. The rate constants are increasing in the following order: ZF2T > ZF2 > ZF1=ZF3 > ZF0. The rate constant exhibits a maximum of 0.022 min<sup>-1</sup> for ZF2T. From the obtained results, it is evident that the produced ZnFe<sub>2</sub>O<sub>4</sub>@TiO<sub>2</sub> nanofibers by electrospinning and PECVD show a very high surface area with mesoporous structure and good properties for the separation of photo-induced electron-hole pairs of TiO<sub>2</sub>. These characteristics significantly increase their photocatalytic activity under visible light, as proved by their very high performance in the degradation of methylene blue under visible light by comparison with previous studies (Table 6).<sup>62, 64-66</sup>

The degradation mechanism, based on all above-mentioned results, the energy band structure of ZnFe<sub>2</sub>O<sub>4</sub>@TiO<sub>2</sub> hetero-interfaces is schematically shown in Figure 8. Zinc ferrite is a p-

type semiconductor, while TiO<sub>2</sub> is an n-type semiconductor. Separately, the band gap of n-type TiO<sub>2</sub> is larger than those of p-type Zinc ferrite, and the Fermi level of ZnFe<sub>2</sub>O<sub>4</sub> is lower than that of TiO<sub>2</sub>. When they are in contact, the Fermi level of TiO<sub>2</sub> is moved down and the Fermi level of ZnFe<sub>2</sub>O<sub>4</sub> is moved up until an equilibrium state is formed. Under light irradiation, electrons and holes are generated in the junction. The charges are driven by the internal electric field (the built-in potential V<sub>bi</sub>). The photogenerated electrons in the conduction band of the p-type ZnFe<sub>2</sub>O<sub>4</sub> cannot transfer to that of n-type TiO<sub>2</sub> because of the barrier established at the junction. Only a small amount can be transferred by the tunnel effect through the electric potential barrier near the junction. The photo-generated holes in TiO<sub>2</sub> can instead migrate from the valence band of n-type TiO<sub>2</sub> to that of p-type ZnFe<sub>2</sub>O<sub>4</sub> because of the gradient established at the junction, so leaving an excess of negative charge in the TiO<sub>2</sub>. These results are important in cationic dyes as MB.<sup>67</sup> The photogenerated holes have a strong oxidizing power to produce OH<sup>•</sup> radicals. In the same time the photogenerated electrons are enough to produce O<sub>2</sub><sup>•-</sup> from molecular oxygen; following this mechanism:



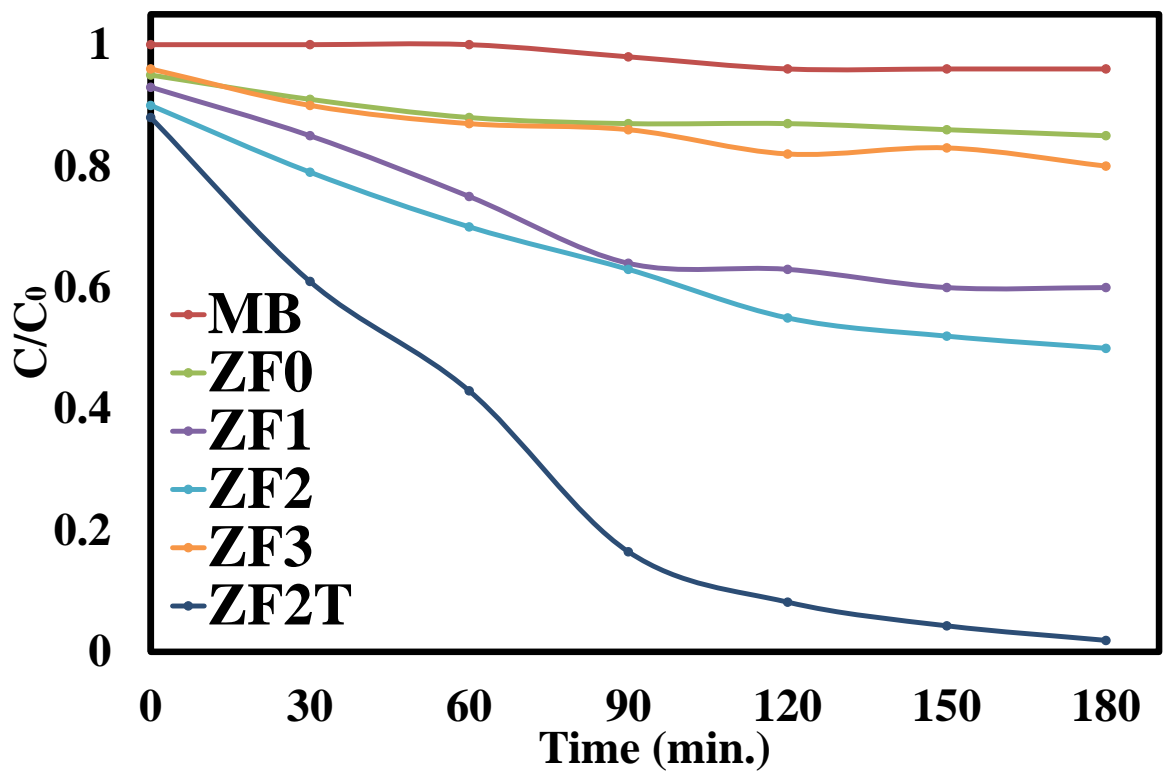


**Figure 6.** Photodegradation of MB by ZF0, ZF1, zinc ferrite, ZF3 and ZF2T nanofibers.

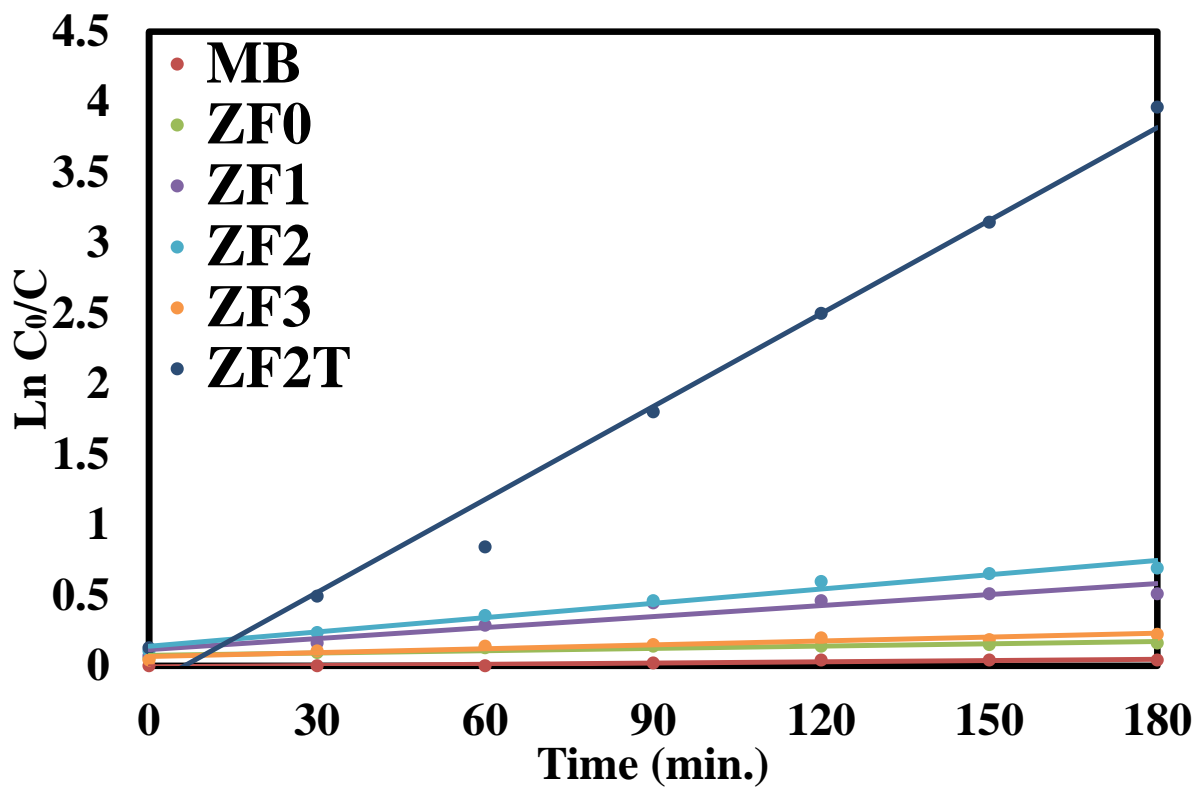


**Figure 7.** Kinetic of MB degradation by ZF0, ZF1, ZF2, ZF3 and ZF2T nanofibers.

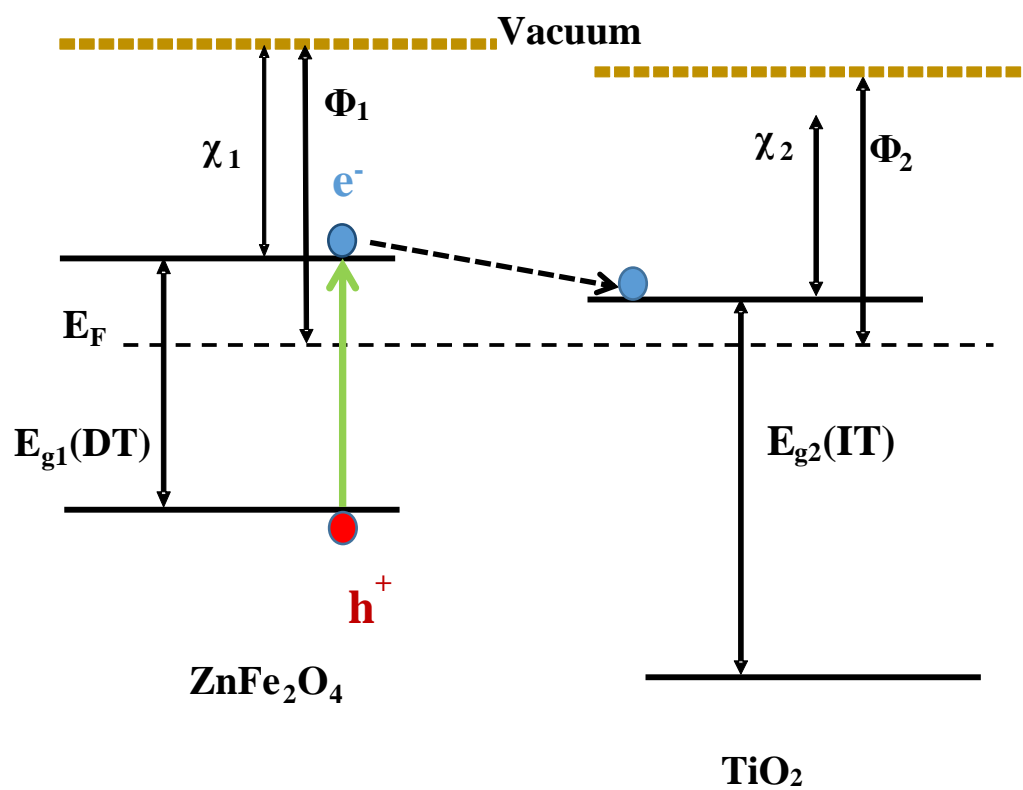


**Figure 8.** The transport mechanism of photogenerated charges in ZF2T

**Table 5.** Kinetic parameters for photocatalytic activities of ZF0, ZF1, ZF2, ZF3 and ZF2T nanofibers.

	$k_a$ (min. <sup>-1</sup> )	$R^2$
MB	0.0003	0.86
ZF0	0.0005	0.85
ZF1	0.0026	0.90

ZF2	0.0034	0.97
ZF3	0.0026	0.94
ZF2T	0.0220	0.98

**Table 6.** Maximum degradation of various photocatalysts for MB under visible light.

Photocatalysts	Weight of catalysts/L	Concentration of MB	Time (h)	Degradation (%)	Ref.
c-NaNbO <sub>3</sub>	1.04 g/L	10 ppm	3 h	87%	<sup>66</sup>
5.0%Zn <sub>3</sub> (OH) <sub>2</sub> V <sub>2</sub> O <sub>7</sub> · <sub>2</sub> H <sub>2</sub> O/g-C <sub>3</sub> N <sub>4</sub>	2 g/L	10 ppm	1 h	90%	<sup>62</sup>
g-C <sub>3</sub> N <sub>4</sub> /TiO <sub>2</sub> -80%	1 g/L	10 ppm	6 h	95%	<sup>65</sup>
mesoporous WO <sub>3</sub>	0.5 g/L	3 ppm	1.2 h	63%	<sup>64</sup>
WO <sub>3</sub> -GO	0.5 g/L	3 ppm	1.2 h	82%	<sup>64</sup>
mesoporous Pt/WO <sub>3</sub>	0.5 g/L	3 ppm	1.2 h	90%	<sup>64</sup>
Pt/ WO <sub>3</sub> -GO	0.5 g/L	3 ppm	1.2 h	94%	<sup>64</sup>
ZnFe <sub>2</sub> O <sub>4</sub> @TiO <sub>2</sub>	1 g/L	20 ppm <sup>*</sup>	3 h	98%	Our work

\* Highest concentration of MB

## CONCLUSION

In this study, by combining the two techniques electrospinning and PECVD, a novel ZnFe<sub>2</sub>O<sub>4</sub>@TiO<sub>2</sub> nanofibers structure with high surface area was successfully manufactured. The photocatalytic activity was evaluated through MB dye degradation under visible light. The prepared zinc ferrite nanofibers with TiO<sub>2</sub> displays the best activity (98% degradation ratio of pollutant) compared to the same sample without TiO<sub>2</sub> (50% degradation ratio of pollutant). Zinc ferrite@TiO<sub>2</sub> acts as p-n junction to keep the electrons on the surface of TiO<sub>2</sub>

inducing enhanced photodegradation of pollutant. Some electrons can accumulate on the surface of  $\text{ZnFe}_2\text{O}_4/\text{TiO}_2$  as confirmed by quenching of photoluminescence. As a conclusion, the zinc ferrite coated with  $\text{TiO}_2$  has a very high potential to enhance the photocatalytic efficiency in the degradation of organic pollutant under visible light.

## ASSOCIATED CONTENT

Supporting Information. Additional figures (Schematic diagram of PECVD reactor, Elemental mapping images and distribution of all elements (a) O, (b) Ti, (c) Fe, (d) Zn for ZF2T nanofibers, Isotherms hysteresis loop and pore size distribution of ZF2 and ZF2T and Adsorption equilibrium of MB) were shown in the supporting information.

## ACKNOWLEDGMENT

Amr Nada acknowledges support from the Science and Technology Development Fund and the “Institut Français en Egypte”.

## REFERENCES

1. Wang, G.; Huang, Y.; Li, G.; Zhang, H.; Wang, Y.; Li, B.; Wang, J.; Song, Y. Preparation of a Novel Sonocatalyst,  $\text{Au/Ni}_2\text{O}_3\text{-Au-Bi}_2\text{O}_3$  Nanocomposite, and Application in Sonocatalytic Degradation of Organic Pollutants. *Ultrason Sonochem.* **2017**, *38*, 335-346.
2. Manavi, N.; Kazemi, A. S.; Bonakdarpour, B. The Development of Aerobic Granules from Conventional Activated Sludge under Anaerobic-Aerobic Cycles and Their Adaptation for Treatment of Dyeing Wastewater. *Chem. Eng. J.* **2017**, *312*, 375-384.
3. Qiu, P.; Thokchom, B.; Choi, J.; Cui, M.; Kim, H.-D.; Han, Z.; Kim, D.; Khim, J. Mesoporous  $\text{TiO}_2$  Encapsulating a Visible-Light Responsive Upconversion Agent for Enhanced Sonocatalytic Degradation of Bisphenol-A. *RSC Adv.* **2016**, *6*, 37434-37442.
4. Wijetunga, S.; Li, X.-F.; Jian, C. Effect of Organic Load on Decolourization of Textile Wastewater Containing Acid Dyes in Upflow Anaerobic Sludge Blanket Reactor. *J. Hazard. Mater.* **2010**, *177*, 792-798.
5. Daneshvar, N.; Salari, D.; Khataee, A. Photocatalytic Degradation of Azo Dye Acid Red 14 in Water on ZnO as an Alternative Catalyst to  $\text{TiO}_2$ . *J. Photochem. Photobiol. A.* **2004**, *162*, 317-322.
6. Zhang, H.; Huang, Y.; Li, G.; Wang, G.; Fang, D.; Song, Y.; Wang, J. Preparation of  $\text{Er}^{3+}:\text{Y}_3\text{Al}_5\text{O}_{12}/\text{WO}_3\text{-KNO}_3$  Composite and Application in Treatment of Methamphetamine under Ultrasonic Irradiation. *Ultrason Sonochem.* **2017**, *35*, 478-488.



7. Gao, J.; Jiang, R.; Wang, J.; Kang, P.; Wang, B.; Li, Y.; Li, K.; Zhang, X. The Investigation of Sonocatalytic Activity of  $\text{Er}^{3+}$ :  $\text{YAlO}_3/\text{TiO}_2\text{-ZnO}$  Composite in Azo Dyes Degradation. *Ultrason Sonochem.* **2011**, *18*, 541-548.
8. Colpini, L. M. S.; Alves, H. J.; dos Santos, O. A. A.; Costa, C. M. M. Discoloration and Degradation of Textile Dye Aqueous Solutions with Titanium Oxide Catalysts Obtained by the Sol–Gel Method. *Dyes Pigm.* **2008**, *76*, 525-529.
9. Nasr, M.; Viter, R.; Eid, C.; Habchi, R.; Miele, P.; Bechelany, M. Enhanced Photocatalytic Performance of Novel Electrospun  $\text{Bn}/\text{TiO}_2$  Composite Nanofibers. *New J. Chem.* **2017**, *41*, 81-89.
10. El-Maghrabi, H.; Ali, H.; Younis, S. Construction of a New Ternary  $\text{A-MoO}_3\text{-WO}_3/\text{CdS}$  Solar Nanophotocatalyst Towards Clean Water and Hydrogen Production from Artificial Wastewater Using Optimal Design Methodology. *RSC Adv.* **2017**, *7*, 4409-4421.
11. Liu, B.; Cheng, K.; Nie, S.; Zhao, X.; Yu, H.; Yu, J.; Fujishima, A.; Nakata, K. Ice-Water Quenching Induced  $\text{Ti}^{3+}$  Self-Doped  $\text{TiO}_2$  with Surface Lattice Distortion and the Increased Photocatalytic Activity. *J. Phys. Chem. C* **2017**, *36*, 19836-19848.
12. Wang, H.; Li, G.; Jia, L.; Wang, G.; Tang, C. Controllable Preferential-Etching Synthesis and Photocatalytic Activity of Porous  $\text{ZnO}$  Nanotubes. *J. Phys. Chem. C* **2008**, *112*, 11738-11743.
13. Anchieta, C. G.; Sallet, D.; Foletto, E. L.; Da Silva, S. S.; Chiavone-Filho, O.; do Nascimento, C. A. Synthesis of Ternary Zinc Spinel Oxides and Their Application in the Photodegradation of Organic Pollutant. *Ceram Int.* **2014**, *40*, 4173-4178.
14. Habibi, M. H.; Habibi, A. H.; Zendejdel, M.; Habibi, M. Dye-Sensitized Solar Cell Characteristics of Nanocomposite Zinc Ferrite Working Electrode: Effect of Composite Precursors and Titania as a Blocking Layer on Photovoltaic Performance. *Spectrochim. Acta Mol. Biomol. Spectrosc.* **2013**, *110*, 226-232.
15. Wang, M.; Sun, Y.; Chen, H.; Zhang, Y.; Wu, X.; Huang, K.; Feng, S. Enhanced Photoelectrochemical Activity of Nanostructured  $\text{ZnFe}_2\text{O}_4$  Thin Films Prepared by the Electrospray Technique. *CrystEngComm.* **2017**, *19*, 772-775.
16. Zhou, X.; Liu, J.; Wang, C.; Sun, P.; Hu, X.; Li, X.; Shimanoe, K.; Yamazoe, N.; Lu, G. Highly Sensitive Acetone Gas Sensor Based on Porous  $\text{ZnFe}_2\text{O}_4$  Nanospheres. *Sens. Actuator B-Chemi.* **2015**, *206*, 577-583.
17. Shao, R.; Sun, L.; Tang, L.; Chen, Z. Preparation and Characterization of Magnetic Core–Shell  $\text{ZnFe}_2\text{O}_4@ \text{ZnO}$  Nanoparticles and Their Application for the Photodegradation of Methylene Blue. *Chem Eng. J.* **2013**, *217*, 185-191.
18. Yao, C.; Zeng, Q.; Goya, G.; Torres, T.; Liu, J.; Wu, H.; Ge, M.; Zeng, Y.; Wang, Y.; Jiang, J.  $\text{ZnFe}_2\text{O}_4$  Nanocrystals: Synthesis and Magnetic Properties. *J. Phys. Chem. C* **2007**, *111*, 12274-12278.
19. Huang, X.; Zhang, J.; Xiao, S.; Sang, T.; Chen, G., Unique Electromagnetic Properties of the Zinc Ferrite Nanofiber. *Mater. Lett.* **2014**, *124*, 126-128.
20. Nam, J.-H.; Joo, Y.-H.; Lee, J.-H.; Chang, J. H.; Cho, J. H.; Chun, M. P.; Kim, B. I. Preparation of  $\text{NiZn}$ -Ferrite Nanofibers by Electrospinning for DNA Separation. *J. Magn. Magn. Mater.* **2009**, *321*, 1389-1392.
21. Xie, J.; Wu, Q.; Zhao, D. Electrospinning Synthesis of  $\text{ZnFe}_2\text{O}_4/\text{Fe}_3\text{O}_4/\text{Ag}$  Nanoparticle-Loaded Mesoporous Carbon Fibers with Magnetic and Photocatalytic Properties. *Carbon* **2012**, *50*, 800-807.
22. Agyemang, F. O.; Kim, H. Electrospun  $\text{ZnFe}_2\text{O}_4$ -Based Nanofiber Composites with Enhanced Supercapacitive Properties. *Mater. Sci. Eng., B* **2016**, *211*, 141-148.
23. Wu, L.; Wu, T.; Mao, M.; Zhang, M.; Wang, T. Electrospinning Synthesis of Ni, Fe Codoped Ultrafine- $\text{ZnFe}_2\text{O}_4/\text{C}$  Nanofibers and Their Properties for Lithium Ion Storage. *Electrochim. Acta* **2016**, *194*, 357-366.
24. Qiu, J.; Wang, C.; Gu, M. Photocatalytic Properties and Optical Absorption of Zinc Ferrite Nanometer Films. *Mater. Sci. Eng., B* **2004**, *112*, 1-4.

25. Zhou, Y.; Fang, S.; Zhou, M.; Wang, G.; Xue, S.; Li, Z.; Xu, S.; Yao, C. Fabrication of Novel ZnFe<sub>2</sub>O<sub>4</sub>/Bioi Nanocomposites and Its Efficient Photocatalytic Activity under Visible-Light Irradiation. *J Alloys Compd.* **2017**, *696*, 353-361.
26. Sun, S.; Yang, X.; Zhang, Y.; Zhang, F.; Ding, J.; Bao, J.; Gao, C. Enhanced Photocatalytic Activity of Sponge-Like ZnFe<sub>2</sub>O<sub>4</sub> Synthesized by Solution Combustion Method. *Prog. Nat. Sci.* **2012**, *22*, 639-643.
27. Harish, K.; Bhojya Naik, H. Solar Light Active ZnFe<sub>2</sub>-Xalxo<sub>4</sub> Materials for Optical and Photocatalytic Activity: An Efficient Photocatalyst. *Int. J. Sci. Res.* **2013**, *1*, 301-307.
28. Wade, J. An Investigation of TiO<sub>2</sub>-ZnFe<sub>2</sub>O<sub>4</sub> Nanocomposites for Visible Light Photocatalysis. University of South Florida, 2005.
29. Nasr, M.; Balme, S.; Eid, C.; Habchi, R.; Miele, P.; Bechelany, M. Enhanced Visible-Light Photocatalytic Performance of Electrospun Rgo/TiO<sub>2</sub> Composite Nanofibers. *J. Phys. Chem. C* **2017**, *121*, 261-269.
30. Schlicht, S.; Assaud, L.; Hansen, M.; Lickleder, M.; Bechelany, M.; Perner, M.; Bachmann, J. An Electrochemically Functional Layer of Hydrogenase Extract on an Electrode of Large and Tunable Specific Surface Area. *J. Mater. Chem. A* **2016**, *4*, 6487-6494.
31. Ren, H.-T.; Yang, Q. Fabrication of Ag<sub>2</sub>O/TiO<sub>2</sub> with Enhanced Photocatalytic Performances for Dye Pollutants Degradation by a Ph-Induced Method. *Appl. Surf. Sci.* **2017**, *396*, 530-538.
32. Zhang, M.; Chen, C.; Ma, W.; Zhao, J. Visible-Light-Induced Aerobic Oxidation of Alcohols in a Coupled Photocatalytic System of Dye-Sensitized TiO<sub>2</sub> and Tempo. *Angew. Chem.* **2008**, *120*, 9876-9879.
33. Su, J.; Zhu, L.; Geng, P.; Chen, G. Self-Assembly Graphitic Carbon Nitride Quantum Dots Anchored on TiO<sub>2</sub> Nanotube Arrays: An Efficient Heterojunction for Pollutants Degradation under Solar Light. *J. Hazard. Mater.* **2016**, *316*, 159-168.
34. Gou, J.; Ma, Q.; Deng, X.; Cui, Y.; Zhang, H.; Cheng, X.; Li, X.; Xie, M.; Cheng, Q. Fabrication of Ag<sub>2</sub>O/TiO<sub>2</sub>-Zeolite Composite and Its Enhanced Solar Light Photocatalytic Performance and Mechanism for Degradation of Norfloxacin. *Chem. Eng. J.* **2017**, *308*, 818-826.
35. Gong, X.-Q.; Selloni, A.; Dulub, O.; Jacobson, P.; Diebold, U. Small Au and Pt Clusters at the Anatase TiO<sub>2</sub> (101) Surface: Behavior at Terraces, Steps, and Surface Oxygen Vacancies. *J. Am. Chem. Soc.* **2008**, *130*, 370-381.
36. Rodrigues, S.; Ranjit, K. T.; Uma, S.; Martyanov, I. N.; Klabunde, K. J. Single-Step Synthesis of a Highly Active Visible-Light Photocatalyst for Oxidation of a Common Indoor Air Pollutant: Acetaldehyde. *Adv. Mater.* **2005**, *17*, 2467-2471.
37. Liu, G.; Zhao, Y.; Sun, C.; Li, F.; Lu, G. Q.; Cheng, H. M. Synergistic Effects of B/N Doping on the Visible-Light Photocatalytic Activity of Mesoporous TiO<sub>2</sub>. *Angew. Chem. Int. Ed.* **2008**, *47*, 4516-4520.
38. Li, D.; Haneda, H.; Hishita, S.; Ohashi, N. Visible-Light-Driven N-F-Codoped TiO<sub>2</sub> Photocatalysts. 1. Synthesis by Spray Pyrolysis and Surface Characterization. *Chem. Mater.* **2005**, *17*, 2588-2595.
39. Wang, X.; Li, T.; Yu, R.; Yu, H.; Yu, J. Highly Efficient TiO<sub>2</sub> Single-Crystal Photocatalyst with Spatially Separated Ag and F- Bi-Cocatalysts: Orientation Transfer of Photogenerated Charges and Their Rapid Interfacial Reaction. *J. Mater. Chem. A* **2016**, *4*, 8682-8689.
40. Xu, Y.; Mo, Y.; Tian, J.; Wang, P.; Yu, H.; Yu, J. The Synergistic Effect of Graphitic N and Pyrrolic N for the Enhanced Photocatalytic Performance of Nitrogen-Doped Graphene/TiO<sub>2</sub> Nanocomposites. *Appl. Catal., B.* **2016**, *181*, 810-817.
41. Lai, C.; Wang, M.-M.; Zeng, G.-M.; Liu, Y.-G.; Huang, D.-L.; Zhang, C.; Wang, R.-Z.; Xu, P.; Cheng, M.; Huang, C. Synthesis of Surface Molecular Imprinted TiO<sub>2</sub>/Graphene Photocatalyst and Its Highly Efficient Photocatalytic Degradation of Target Pollutant under Visible Light Irradiation. *Appl. Surf. Sci.* **2016**, *390*, 368-376.

42. Qin, N.; Xiong, J.; Liang, R.; Liu, Y.; Zhang, S.; Li, Y.; Li, Z.; Wu, L. Highly Efficient Photocatalytic H<sub>2</sub> Evolution over MoS<sub>2</sub>/CdS-TiO<sub>2</sub> Nanofibers Prepared by an Electrospinning Mediated Photodeposition Method. *Appl. Catal., B* **2017**, *202*, 374-380.
43. El-Maghrabi, H. H.; Nada, E. A.; Soliman, F. S.; Moustafa, Y. M.; Amin, A. E.-S. One Pot Environmental Friendly Nanocomposite Synthesis of Novel TiO<sub>2</sub>-Nanotubes on Graphene Sheets as Effective Photocatalyst. *Egypt. J. Pet.* **2016**, *25*, 575-584.
44. Pavlenko, M.; Coy, E.; Jancelewicz, M.; Załęski, K.; Smyntyna, V.; Jurga, S.; Iatsunskyi, I. Enhancement of Optical and Mechanical Properties of Si Nanopillars by Al<sub>2</sub>O<sub>3</sub> Coating. *RSC Adv.* **2016**, *6*, 97070-97076.
45. Nasr, M.; Viter, R.; Eid, C.; Warmont, F.; Habchi, R.; Miele, P.; Bechelany, M. Synthesis of Novel ZnO/ZnAl<sub>2</sub>O<sub>4</sub> Multi Co-Centric Nanotubes and Their Long-Term Stability in Photocatalytic Application. *RSC Adv.* **2016**, *6*, 103692-103699.
46. Viter, R.; Abou Chaaya, A.; Iatsunskyi, I.; Nowaczyk, G.; Kovalevskis, K.; Erts, D.; Miele, P.; Smyntyna, V.; Bechelany, M. Tuning of ZnO 1D Nanostructures by Atomic Layer Deposition and Electrospinning for Optical Gas Sensor Applications. *Nanotechnology* **2015**, *26*, 105501.
47. Bechelany, M.; Drobek, M.; Vallicari, C.; Abou Chaaya, A.; Julbe, A.; Miele, P. Highly Crystalline MOF-Based Materials Grown on Electrospun Nanofibers. *Nanoscale* **2015**, *7*, 5794-5802.
48. Selloum, D.; Abou Chaaya, A.; Bechelany, M.; Rouessac, V.; Miele, P.; Tingry, S., A Highly Efficient Gold/Electrospun Pan Fiber Material for Improved Laccase Biocathodes for Biofuel Cell Applications. *J. Mater. Chem. A* **2014**, *2*, 2794-2800.
49. Song, H.; Jiang, H.; Liu, X.; Meng, G. Efficient Degradation of Organic Pollutant with WO<sub>3</sub> Modified Nano TiO<sub>2</sub> under Visible Irradiation. *J. Photochem. Photobiol. A* **2006**, *181*, 421-428.
50. Du, P.; Song, L.; Xiong, J.; Cao, H. Photocatalytic Degradation of Rhodamine B Using Electrospun TiO<sub>2</sub> and ZnO Nanofibers: A Comparative Study. *J. Mater. Sci.* **2013**, *48*, 8386-8392.
51. Li, Y.; Dai, G.; Zhou, C.; Zhang, Q.; Wan, Q.; Fu, L.; Zhang, J.; Liu, R.; Cao, C.; Pan, A. Formation and Optical Properties of ZnO: ZnFe<sub>2</sub>O<sub>4</sub> Superlattice Microwires. *Nano Res.* **2010**, *3*, 326-338.
52. Zamiri, R.; Salehizadeh, S.; Ahangar, H. A.; Shabani, M.; Rebelo, A.; Kumar, J. S.; Soares, M.; Valente, M.; Ferreira, J. Optical and Magnetic Properties of ZnO/ZnFe<sub>2</sub>O<sub>4</sub> Nanocomposite. *Mater. Chem. Phys.* **2017**, *192*, 330-338.
53. Thota, S.; Kashyap, S. C.; Sharma, S. K.; Reddy, V. Micro Raman, Mossbauer and Magnetic Studies of Manganese Substituted Zinc Ferrite Nanoparticles: Role of Mn. *J. Phys. Chem. Solids* **2016**, *91*, 136-144.
54. Vahtrus, M.; Šutka, A.; Vlassov, S.; Šutka, A.; Polyakov, B.; Saar, R.; Dorogin, L.; Löhmus, R. Mechanical Characterization of TiO<sub>2</sub> Nanofibers Produced by Different Electrospinning Techniques. *Mater. Charact.* **2015**, *100*, 98-103.
55. Yan, J.; Gao, S.; Wang, C.; Chai, B.; Li, J.; Song, G.; Chen, S. A Facile Electrospinning and Direct Annealing Method for the Fabrication of Multi-Porous ZnFe<sub>2</sub>O<sub>4</sub> Nanotubes with Enhanced Photocatalytic Activity. *Mater. Lett.* **2016**, *184*, 43-46.
56. Štengl, V.; Henych, J.; Slušná, M. H-BN-TiO<sub>2</sub> Nanocomposite for Photocatalytic Applications. *J. Nanomater.* **2016**, *2016*, 22.
57. Lindberg, J. D.; Snyder, D. G. Determination of the Optical Absorption Coefficient of Powdered Materials Whose Particle Size Distribution and Refractive Indices Are Unknown. *Appl. Opt.* **1973**, *12*, 573-578.
58. Viter, R.; Iatsunskyi, I.; Fedorenko, V.; Tumenas, S.; Balevicius, Z.; Ramanavicius, A.; Balme, S.; Kempinski, M.; Nowaczyk, G.; Jurga, S.; et al. Enhancement of Electronic and Optical Properties of ZnO/Al<sub>2</sub>O<sub>3</sub> Nanolaminate Coated Electrospun Nanofibers. *J. Phys. Chem. C* **2016**, *120*, 5124-5132.
59. Liu, X. Y.; Zheng, H. W.; Li, Y.; Zhang, W. F. Factors on the Separation of Photogenerated Charges and the Charge Dynamics in Oxide/ZnFe<sub>2</sub>O<sub>4</sub> Composites. *J. Mater. Chem. C* **2013**, *1*, 329-337.

60. Pawar, R. C.; Lee, C. S. Chapter 1 - Basics of Photocatalysis. In *Heterogeneous Nanocomposite-Photocatalysis for Water Purification*, William Andrew Publishing: Boston, 2015; pp 1-23.
61. Liu, H.; Hao, H. Y.; Xing, J.; Dong, J. J.; Zhang, Z. L.; Zheng, Z. Y.; Zhao, K. Enhanced Photocatalytic Capability of Zinc Ferrite Nanotube Arrays Decorated with Gold Nanoparticles for Visible Light-Driven Photodegradation of Rhodamine B. *J. Mater. Sci.* **2016**, *51*, 5872-5879.
62. Xu, X. M.; Li, S. D.; Wang, X. L.; Ma, Y. T.; Wang, X. H.; Gao, K. Fabrication and Characterization of Ca<sub>2</sub>Fe<sub>2</sub>O<sub>5</sub> Nanofibers Photocatalyst by Sol-Gel Assisted Electrospinning at Low-Temperature. *Mater. Lett.* **2015**, *143*, 75-79.
63. Cheng, P.; Li, W.; Liu, H.; Gu, M.; Shangguah, W. Influence of Zinc Ferrite Doping on the Optical Properties and Phase Transformation of Titania Powders Prepared by Sol-Gel Method. *Mater. Sci. Eng. A* **2004**, *386*, 43-47.
64. Ismail, A. A.; Faisal, M.; Al-Haddad, A. Mesoporous WO<sub>3</sub>-Graphene Photocatalyst for Photocatalytic Degradation of Methylene Blue Dye under Visible Light Illumination. *J. Environ. Sci.* **2017**, DOI: 10.1016/j.jes.2017.05.001
65. Li, C.; Sun, Z.; Xue, Y.; Yao, G.; Zheng, S. A Facile Synthesis of G-C<sub>3</sub>N<sub>4</sub>/TiO<sub>2</sub> Hybrid Photocatalysts by Sol-Gel Method and Its Enhanced Photodegradation Towards Methylene Blue under Visible Light. *Adv. Powder Technol.* **2016**, *27*, 330-337.
66. Wang, L.; Gu, H. S.; He, J.; Zhao, T. T.; Zhang, X. W.; Xiao, C.; Liu, H.; Zhang, X. H.; Li, Y. B. Scale Synthesized Cubic Nanbo<sub>3</sub> Nanoparticles with Recoverable Adsorption and Photodegradation for Prompt Removal of Methylene Blue. *J. Alloys. Compd.* **2017**, *695*, 599-606.
67. Scuderi, V.; Amiard, G.; Sanz, R.; Boninelli, S.; Impellizzeri, G.; Privitera, V. TiO<sub>2</sub> Coated CuO Nanowire Array: Ultrathin P-N Heterojunction to Modulate Cationic/Anionic Dye Photo-Degradation in Water. *Appl. Surf. Sci.* **2017**, *416*, 885-890.

# TOC Graphic

